Compact multi-aperture imaging with high-angular-resolution

Guillem Carles,[1] Gonzalo Muyo,[2] Nicholas Bustin,[3] Andrew Wood,[3] and Andrew R. Harvey[1,*]

[1] *School of Physics and Astronomy, University of Glasgow, United Kingdom*
[2] *School of Engineering and Physical Sciences, Heriot-Watt University, United Kingdom*
[3] *Qioptiq Ltd, St Asaph, United Kingdom*
**Corresponding author: andy.harvey@glasgow.ac.uk*

Received Month X, XXXX; revised Month X, XXXX; accepted Month X, XXXX; posted Month X, XXXX (Doc. ID XXXXX); published Month X, XXXX

Previous reports have demonstrated that it is possible to emulate the imaging function of a single conventional lens with an NxN array of identical lenslets to provide an N-fold reduction in imaging-system track length. This approach limits the application to low-resolution imaging. We highlight how using an array of dissimilar lenslets, with an array width that can be much wider than the detector array, high-resolution super-resolved imaging is possible. We illustrate this approach with a ray-traced design and optimization of a long-wave infrared system employing a 3x3 array of free-form lenslets to provide a four-fold reduction in track length compared to a baseline system. Simulations of image recovery show that recovered image quality is comparable to that of the baseline system.

OCIS codes: (100.3020) Image reconstruction-restoration; (100.6640) Superresolution; (110.1758) *Computational imaging.*
http://dx.doi/org/10.1364/AO.99.099999

1. Introduction

The physical dimensions of conventional imaging systems are dominated by the interplay between fundamental parameters such as field-of-view, angular resolution and detector size, and in particular by the focal length of the lens. Multi-aperture (MA) imaging [1] involves the replacement of the function of a single conventional lens by an array of lenses of shorter focal length to record an array of images onto a single detector array that are combined using super-resolution algorithms to yield a single high-resolution image. When the angular resolution is limited by the size of the detector pixels, this can enable a significant reduction in imaging-system track length without sacrificing angular resolution. The use of a single detector array with an array of nominally identical lenses, as previously reported [2-6], limits the maximum aperture of the lens array to the width of the detector array and hence the benefit for MA imaging has previously been restricted to low-angular-resolution systems. We describe how the use of arrays of dissimilar lenses, some operating off-axis, but with an overall width wider than the detector array, enables the length-reduction benefit of MA imaging to be attained for high-resolution imaging. We demonstrate the concept with an example design and simulation of imaging performance in the long-wavelength infrared (LWIR) band in which the length of the lens is reduced by a factor of four whilst maintaining imaging performance.

In general, substitution of a single full-aperture lens by a MA system consisting of $N\times N$ smaller-aperture imaging channels allows an N-fold reduction in focal length and hence in the lens track-length. Focal-length reduction decreases the object-space angular sampling frequency of the detector array (that is, the detector sampling frequency projected onto the scene), but since $N\times N$ images are recorded with, in general, dissimilar sampling phases, super-resolution techniques may be used to effectively maintain the higher sampling frequency of the single-aperture imaging system [7]. This is true only if (1) sampling is non-redundant between image channels and (2) if the reduced diffraction-limited angular resolution of the smaller image channels is not too low. On the first issue; MA imaging relies on aliasing to encode angular-frequency information lying above the Nyquist frequency within the baseband of recorded images, and on non-redundancy between images to enable super-resolution to recover the angular-frequency components between the Nyquist frequency and the optical cut-off from baseband images. The sampling phase and redundancy varies with range and at certain ranges there could, for a perfectly manufactured system, be significant redundancy between channels and super-resolution would be ineffective. In practice however, typical manufacturing tolerances tend to randomize sampling phase, maintaining the effectiveness of super-resolution with range [8]. On the second issue; the N-fold reduction in width of a lens aperture also reduces the diffraction-limited angular resolution by a factor N and thus MA imaging can maintain the angular resolution of a single-aperture imaging system only for small N. MA imaging have previously been used to improve compactness, but its application has been restricted to low-angular resolution imaging [2-6]. This restriction is associated with the use of arrays of identical lenslets, whereas we describe here how use of arrays of

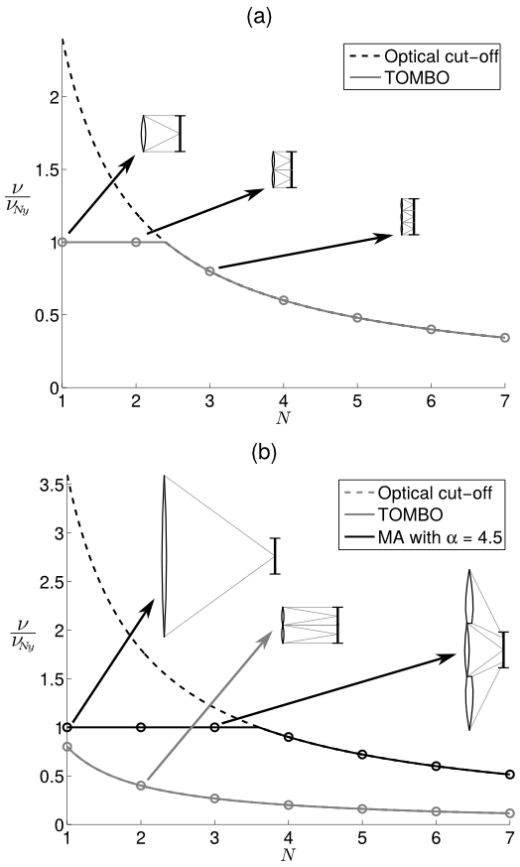

Fig. 1. Variation of normalized system cutoff frequency ν_c^{sys} with N for representative MA systems, for (a) f=33mm with α=1 and (b) f=100mm with α=1 (grey line) and α=4.5 (black line). The drawings depict the gain in compactness. Pixel pitch is p=25μm and λ=10μm.

larger, but necessarily dissimilar lenslets, offers the potential of reduced track-length for high-angular-resolution imaging. A *quid pro quo* for this advantage is the increased complexity of image recovery associated with spatial variations in imaging characteristics.

Use of MA architectures is also found in the so-called compound-eye cameras, for example using prisms or dissimilar lenslets to steer light beams to extend the field-of-view by stitching the acquired subimages [9-12]. These approaches include use of dissimilar lenses to increase non-redundancy [6] or lenslet arrays exceeding detector width [11, 12]; however, none of these demonstrate reduced track length for arbitrarily high angular resolution. MA imaging is also a feature of light-field imaging, such as is found in plenoptic cameras [13, 14] where a lenslet array is placed close to the image plane. By reimaging the differing parts of the pupil, these techniques have similarities with MA imaging, including the ability to digitally simulate reduced depth of field, but improved compactness has not been reported. However, two characteristics of plenoptic imaging are shared with the approach presented here: a lower sampling rate results in aliasing that enables digital super-resolution [14-17], and the effective size of the aperture is reduced leading to a reduction in optical resolution.

We consider here how high-resolution MA imaging can be achieved using a lens array that is wider than the detector array, which enables high-resolution MA imaging for common practical systems for the first time. This requires that the outer lenses of the lens array operate off-axis and generally introduces dissimilar distortions between channels that provide, in principle, the benefit of breaking the redundancy to provide consistent super-resolution performance [8]. The arrangement of this article is as follows: section 2 offers a physical insight into the fundamental design trade-offs; section 3 presents an example optimized and ray-traced design for a LWIR imaging system employing a 3x3 array of lenses with an aperture 4.5 times wider than the detector, and shows simulated imaging performance compared with a conventional baseline system; we conclude in section 4.

2. Multi-aperture design

The salient aim in the design of a MA imaging system is reduction of physical length while maintaining imaging performance. We consider here the replacement of a single lens of focal length f and diameter D by an $N\times N$ array of lenslets of focal length f/N and diameter D/N. We will consider first the configuration reported in [1] and termed *Thin Observation Module by Bound Optics* (TOMBO) where the lens-array width D is limited to be equal to the detector width. This restriction limits application of this concept to low-angular-resolution imaging. We will then consider how the use of a larger aperture $D' = \alpha D$ allows higher angular resolutions to be achieved. Traditional TOMBO-like designs thus correspond to MA systems with $N \geq 2$ and $\alpha \leq 1$.

The focal length of each subsystem is reduced by a factor N for a MA system and the aim is hence to maximally increase N without degrading angular resolution. The width of the point-spread function (PSF) at the detector is the same regardless of N because focal ratio is preserved, but since the magnification is increased by a factor N, the angular-resolution limit due to diffraction is reduced by N. We describe resolution in angular frequencies to allow comparison for different N. We thus now consider how the angular resolution varies in terms of the system angular cutoff frequency of the imaging system. For the baseline N=1 imager, the angular optical-cutoff frequency is $\nu_o = \alpha D / \lambda$, where λ is the wavelength, but for detector-limited imaging, the system cutoff frequency is the Nyquist angular frequency, $\nu_{Ny} = f / 2p$, where p is pixel pitch. For a MA system, the Nyquist angular frequency of each channel is reduced to $\nu_{Ny}^{ch} = \nu_{Ny} / N$ but the effective Nyquist frequency of the super-resolved image is identical to that of the baseline imager, provided the sampling is non redundant. Throughout this paper we refer to ν_{Ny} as the Nyquist angular frequency of the baseline imaging system. The optical cutoff frequency for each lenslet is $\nu_o^{ch} = \alpha D / (\lambda N)$ and the system cutoff frequency, ν_c^{sys}, is therefore the lesser of ν_{Ny} and ν_o^{ch}; that is,

$$\nu_c^{\mathrm{sys}} = \begin{cases} \dfrac{\alpha D}{N\lambda} & \text{for } N \geq \dfrac{2\alpha D p}{f\lambda} \\ \dfrac{f}{2p} & \text{for } N < \dfrac{2\alpha D p}{f\lambda} \end{cases} \qquad (1)$$

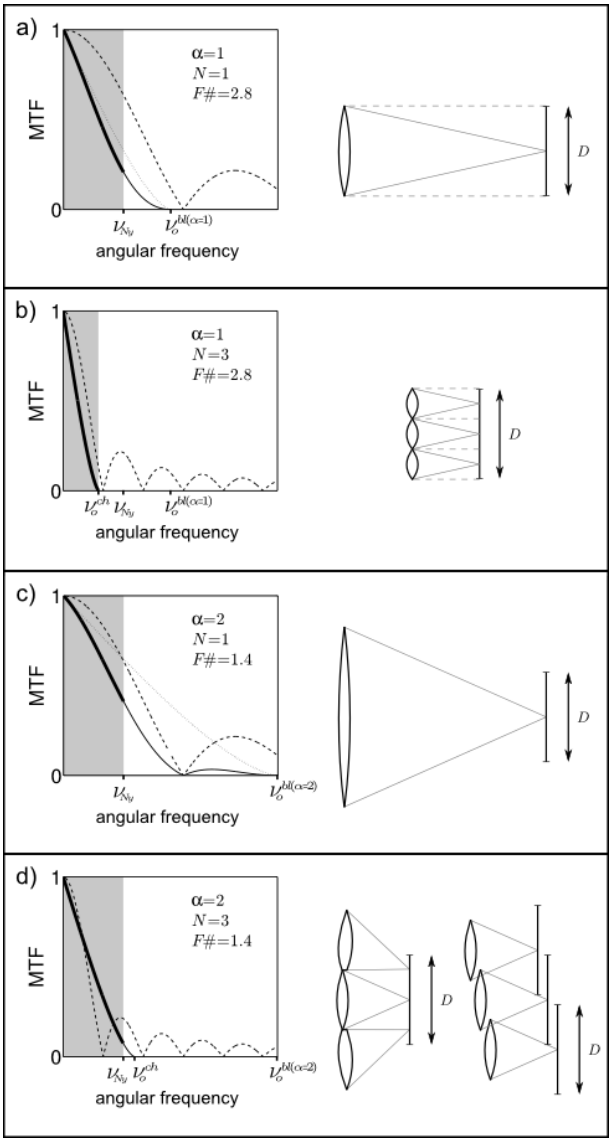

Fig. 2. Schematic representations of imaging system and associated MTFs, for a conventional system (a,c) and its N=3 MA equivalent (b,d). In (a,b) α=1 whereas in (c,d) α=2. In each graph the dashed, dotted and solid lines show the pixel, optical and total MTF respectively. The shaded area indicates the baseband of the image for which the frequencies falling on the detector are below the Nyquist frequency and the thicker solid line shows the total MTF restricted to the system cut-off defined in Eq. (1). Baseline focal length is f=70mm, λ=10μm and pixel pitch is p=25μm. Note that ν_{Ny} as indicated for both N=1 and N=3 corresponds to the Nyquist angular frequency of the baseline system.

The variation of normalized cutoff frequency ν_c^{sys}/ν_{Ny} with N is illustrated for a representative MA imaging system with α=1 in Fig. 1(a) and for a system with identical detector parameters, but a three-fold longer focal length in Fig. 1(b) for the cases of α=1 and α=4.5. In the former example, angular resolution is maintained for N=2, providing a halving in focal length and track length, but for N>2, diffraction increases and reduces angular resolution. For the longer-focal-length example in Fig. 1(b), when α=1, diffraction reduces resolution for N>1 and MA imaging is unattractive, but for α=4.5, MA imaging offers a reduction in f and track length while maintaining resolution for N≤3. This is the advantage that is exploited in this article. For $\alpha > 1$ off-axis imaging using non-axial lenslets is necessary and these introduce variations in distortion between lenslets, which has the felicitous advantage of introducing non-redundancy between the sampling of the images by different image channels.

From Eq. (1) the focal length for which MA imaging (N≥2) enables the system cutoff to equal that of a baseline imager is $f' \le 2\alpha Dp/(N\lambda)$. For a system with α=1, employing a LWIR detector with 640×640 pixels at 25μm pitch, MA imaging with N=2 offers a length reduction without sacrificing angular resolution only for f'≤40mm. Recent MA implementations found in the literature correspond to α=1 and are subject to this constraint of low-resolution imaging [2-6].

We depict in Fig. 2 the schematic layout for systems with α={1,2} and N={1,3} and the associated MTFs. This relatively small width of lenslet array is used simply for clarity of presentation. In these examples, f/D=2.8, λ=10μm, and p=25μm. For the baseline system in Fig. 2(a), f=70 mm and angular resolution is detector limited and so $\nu_c^{sys}=\nu_{Ny}$=1.4mrad^{-1}. For the N=3 MA imager in Fig. 2(b), super-resolution construction of the final image yields an effective Nyquist frequency equal to that of the baseline system, but the diffraction limit is reduced to $\nu_c^{sys}=\nu_o^{ch}$=0.83mrad^{-1}; that is the constraint for α=1 limits angular resolution to less than that of the baseline system. The baseline and N=3 MA systems for a lenslet array wider than the detector are shown in Fig. 2(c) and Fig. 2(d) for system parameters identical to Fig. 2(a) and Fig. 2(b), except the lens diameter, which is doubled and so f/D=1.4 and α=2. Although ν_o for this baseline system is doubled, ν_{Ny} is 1.4mrad as for Fig. 2(a) and so the main effects on image quality are an increase in the magnitude of alias artifacts and a quadrupling of pixel étendue. In Fig. 2(d) we depict two configurations for achieving the length-reduction advantage of MA imaging while maintaining the high angular resolution and numerical aperture of the baseline system. In the configuration on the left, the use of an array larger than the single detector necessitates that non-axial lenses are used off axis and this introduces additional benefits and challenges as discussed below. For this system, the optical cutoff frequency is reduced by a factor of three to ν_o^{ch}=1.67mrad^{-1} while super resolution maintains a nominal effective Nyquist frequency of ν_{Ny} of 1.4/mrad^{-1}. That is, the use of a lenslet array wider than the detector, necessarily employing off-axis lenses, enables the length-reduction of MA imaging to be obtained for high-resolution imaging. For completeness, in the right image of Fig. 2(d), we depict the simpler case where multiple independent detector cameras are used so that all lenses are used on-axis [18]. This latter implementation is attractive when detector arrays are low cost and relies on imperfect tolerancing to statistically break redundancy in sampling of the image.

In the graphs in Fig. 2, system MTFs are denoted by thick solid lines; in Fig. 2(a,c) it is the combined pixel and optical MTFs, whereas in Fig. 2(b,d) it is assumed that super-resolution is able to recover the system MTF to the diffraction-limited optical MTF of a single channel. The null in the pixel MTF at the sampling frequency (νs=2νNy/N) indicates irrecoverable information, however, in practice variations in the null location occurs between dissimilar channels enabling some improvement of recovery of information in the region of nulls. This can be achieved by slightly varying focal length on different channels and, as described here, from the dissimilar optical distortions introduced by dissimilar lenslets used on axis and off axis. In

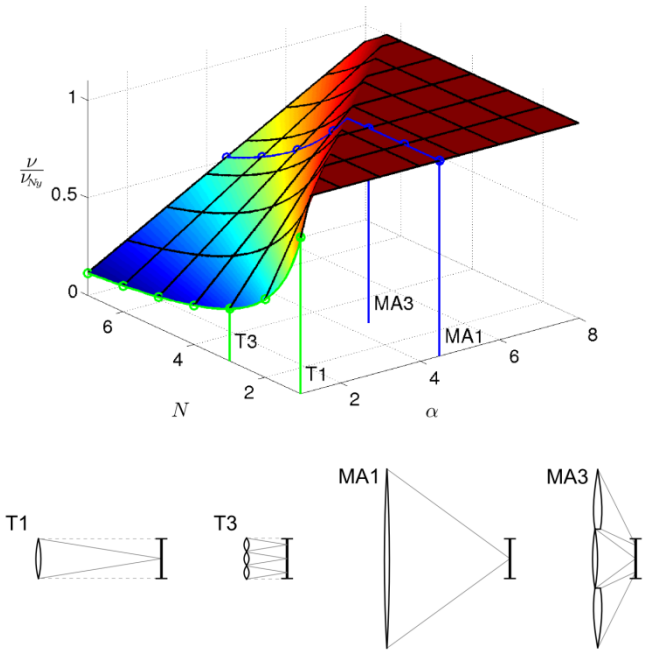

Fig. 3. Representative plot of normalized system bandwidth against number of channels N and relative aperture increase α. Focal length for N=1 is f=100mm, λ=10μm and pixel pitch is p=25μm. The intersection of the curve with the α=1 plane corresponds to the established concept for TOMBO. The diagrams on the bottom correspond to selected points in the design space: T1 and T3 correspond to baseline N=1 and equivalent N=3 designs for α=1; MA1 and MA3 are baseline N=1 and MA N=3 designs with α=4.5.

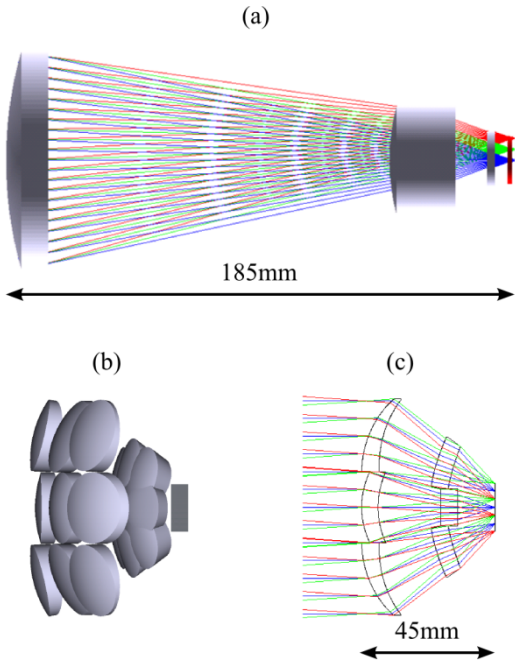

Fig. 4. Layout of the (a) baseline and (b,c) MA systems. (b) shows the optimized front and back lenslets in front of the detector and (c) the ray trace for several fields in the vertical profile of the system.

Tab. 1, the systems from Fig. 2 are summarized in terms of the advantages and disadvantages of each approach.

We describe now the design of a MA imaging system that is equivalent to a specific baseline imager. Fig. 3 depicts the variation in normalized system cutoff frequency with α and N where the sections of constant α correspond to the plots in Fig. 1(b). The maximal reduction in track length is obtained by the selection of the highest value for N that does not reduce the highest angular cutoff frequency. From Eq. (1), this can be written as

$$N^* = \left\lfloor \frac{2\alpha n p^2}{\lambda f} \right\rfloor \qquad (2)$$

where $\lfloor x \rfloor$ denotes integer part of x and n is the number of pixels across the detector array. The plateau region of the plot corresponds to combinations of α and N for which MA imaging enables an optical system cutoff frequency ν_c^{sys} equal to that of the baseline imager. Finally the profile at α=1 shows how a TOMBO-based approach is unattractive for large focal lengths since it results in a reduction in cutoff frequency, ν_o, associated with the high f-number.

3. Design example for LWIR imaging

In this Section we present a detailed optical design to illustrate and demonstrate the concept of high-resolution MA imaging in the LWIR band including a ray-traced simulation of imaging performance. High-resolution MA imaging is not fundamentally restricted to any particular band, but is particularly important for thermal infrared imaging for which the higher aliasing ratios associated with larger pixels (measured in wavelengths) and compactness afforded by MA imaging offers a more significant benefit. The reference baseline system is shown in Fig. 4(a); it consists of a f/1.6 germanium Petzval lens with f=114mm and

Table 1. Comparison of offered benefits of the different imaging approaches. Nominal specifications are as of Fig. 2: wavelength is λ=10μm, pixel pitch is p=25μm and detector size is D=25mm.

	f(mm)	Length×Width of lens array[a] (mm)	ν_c^{sys} (mrad^{-1})	Benefit	Disadvantages
Conventional	70	83×50	1.4	No image processing required	Long track length
TOMBO	23.3	28×25	0.83	Reduced length	Image processing required Limited to low angular resolution
Proposed MA	23.3	28×50	1.4	Reduced length	Image processing required

[a]Based on the same telephoto ratio in each case and overall aperture(s) size.

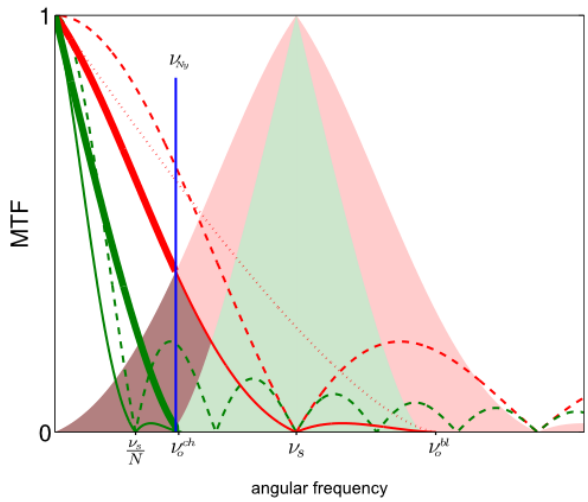

Fig. 5. MTF plots of conventional (red) and MA (green) imaging systems. Dotted, dashed and solid lines are optical, pixel and combined MTFs respectively and the thicker solid lines denote system MTFs (in the MA system it is assumed that super-resolution recovers the diffraction limit). The shaded areas show the first spectral replicas of each system (replication of the system MTFs respectively) and the darker red area shows the overlapped aliased content for the baseline imager. For the baseline system ν_o=7.2mrad^{-1} and ν_s=2ν_{Ny}=4.56mrad^{-1} whereas for the N=3 MA system ν_o^{ch}=2.4mrad^{-1}.

D=72mm together with and a 640×640-pixel detector array with p=25μm, giving 8 degrees full field of view and total system-length of 185mm. Therefore, α=4.5, $\nu_{Ny}=f/(2p)$=2.28mrad^{-1} and for λ=10μm, ν_o=7.2mrad^{-1}. From Eq. (2) we select N=3. The optical, pixel and system MTFs for the baseline system and its MA equivalent are depicted in Fig. 5 in the diffraction-limited approximation. The baseline system MTF is the product of the optical and pixel MTFs and with a system cutoff limited to ν_{Ny}. In the MA counterpart, the angular sampling frequency of each channel is a factor of three lower, but super-resolution of the 3×3 array yields an effective angular sampling frequency equal to that of the baseline system and so $\nu_c^{sys}=\nu_{Ny}$=2.28mrad^{-1} for both baseline and MA systems, which is approximately equal to the optical cutoff frequency ν_o^{ch}=2.4mrad^{-1}. It is possible therefore for SR image recovery to yield a system MTF with the same cutoff as the baseline system, and with a similar MTF to that of a diffraction-limited lenslet, provided that the MTFs vary sufficiently between lenslets to prevent loss of information close to the nulls of pixel-transfer function (when mapped into angle space). This is depicted as the solid green line in Fig. 5. Although the diffraction limit will not be achieved in practice due to strong suppression by the pixel MTF around its null, the system cutoff frequency will approach the diffraction cutoff. Red and green shaded areas in Fig. 5 represent the first spectral replicas of the baseline and MA system MTFs respectively showing how aliasing in the single-aperture case corrupts the baseband signal ($\nu<\nu_{Ny}$) [8]. On the other hand, as can be appreciated from Fig. 5, the reduced MTF for the MA system introduces some reduction in sensitivity, together with the arguably beneficial mitigation of the aliased response.

A. Optical design

The MA equivalent of the baseline system consists of nine germanium front elements and nine germanium rear elements as illustrated in Fig. 4(b). Each of the two-element lenslet

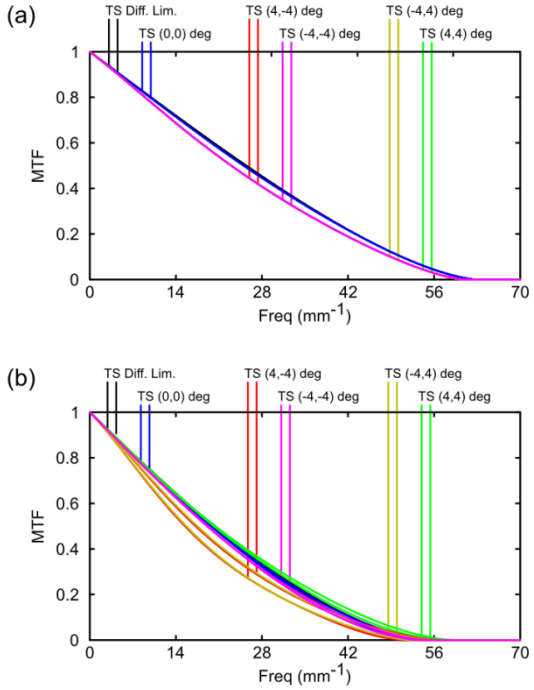

Fig. 6. Monochromatic MTF for the (a) central and (b) corner channels. Tangential (T) and sagittal (S) MTFs are plotted.

subsystems has been independently optimized using free-form surfaces, thus the system forms nine under-sampled images with diffraction-limited performance on a single detector. MTFs for the central and corner channels are plotted in Fig. 6 for various fields and show agreement with the plots for the Fourier-optic approximations shown in Fig. 5.

Since the subsystems are not down-scaled versions of the baseline system, the reduction in focal and track lengths will generally be different; in this case the track-length reduction is four, rather than the factor of three one might expect from the simplified arguments presented above. This improvement in track-length reduction arises from the additional optimization freedom provided by the use of free-form surfaces for the rear lens elements, which has provided an improved telephoto ratio.

A LWIR scene and a simulation of its acquisition by the proposed MA system are shown in Fig. 7. This rigorous simulation was conducted by ray tracing using *Zemax*®. Non-redundant sampling across channels is ensured by the inherent geometric distortions introduced by the imaging systems, which vary from channel to channel as is clear in the detected image in Fig. 7. Both baseline and MA imaging systems have been optimized to operate at infinite conjugates.

As can be appreciated in Fig. 4(b), oblique rays entering each of the nine front lenses can enter neighboring lenses in the rear elements and this stray light can be prevented by baffling. For convenience, in these simulations, the equivalent baffling function is achieved by shading the front apertures. There is an associated reduction in the optical MTF in certain directions, but, since these directions vary between channels the impact on final imaging performance is very small.

B. Image recovery

A high-resolution image is constructed using a super-resolution model that accounts for imaging distortion, blurring by lenslet PSFs and sampling introduced in each channel [19-21]. The forward model can be described by,

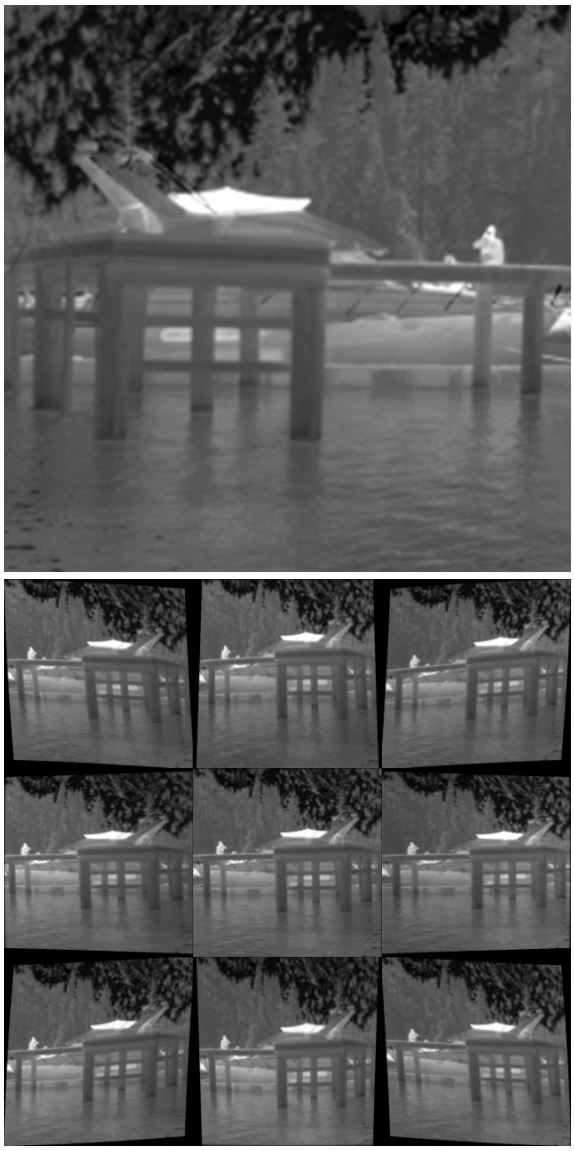

Fig. 7. High-resolution scene (top) and full frame acquired with the MA system (bottom). (Original image courtesy of Sierra Pacific Innovations Corp.)

$$\mathbf{y}_k = \mathbf{D}_k \mathbf{H}_k \mathbf{W}_k \mathbf{x} + \mathbf{e}_k \qquad 1 \le k \le 9 \tag{3}$$

where each vector $\mathbf{y}_k$ denotes the lexicographically-ordered low-resolution image recorded for channel k, $\mathbf{x}$ is the high resolution object, matrices $\mathbf{D}$, $\mathbf{H}_k$ and $\mathbf{W}_k$ denote decimation, blurring, and geometric warping operations respectively, and vector $\mathbf{e}_k$ is additive noise that corrupts data at the point of detection.

The blurring and geometric warping matrices are calculated from the simulated PSF, which has a field-dependence which we incorporate in $\mathbf{H}_k$, and distortion from the *Zemax*® model. It is important to note that, for a manufactured system, errors in misalignments and tolerances in the fabrication process would arise; however a calibration of such system from PSF and distortion measurements is possible and hence would be included in Eq. (3). Thus, the expected impact of misalignment errors and tolerances in fabrication is very small. Misalignments and tolerances in fabrication can also have an impact on the achieved non-redundancy; however this will also be reduced due to the differing spatial distortion between channels. Equivalently, the system can also yield high-quality finite-conjugate imaging following range-dependent calibration of the sampling offsets between imagers [8].

Concatenating Eq. (3) across channels the forward model of the system can be written as a classic restoration problem model,

$$\mathbf{y} = \mathbf{M}\mathbf{x} + \mathbf{e} \tag{4}$$

Due to its high dimensionality it is not feasible to uniquely invert the system matrix $\mathbf{M}$ to obtain an estimate of $\mathbf{x}$, denoted by $\hat{\mathbf{x}}$, and instead iterative algorithms are preferred for inversion [22-27]. In this work the maximum likelihood estimator

$$\hat{\mathbf{x}}_{i+1} = \mathrm{diag}\{\hat{\mathbf{x}}_i\}\mathbf{M}^{\mathrm{T}}\left(\mathrm{diag}\{\mathbf{M}\hat{\mathbf{x}}_i\}\right)^{-1}\mathbf{y} \tag{5}$$

is used, where $\mathbf{M}^{\mathrm{T}}$ denotes the transpose of $\mathbf{M}$, $\hat{\mathbf{x}}_i$ is the iterative estimation, and the vector $\mathbf{x}$ populates the elements of the diagonal matrix diag{$\mathbf{x}$}. This resembles Lucy-Richardson iterative deconvolution for Poisson-distributed noise [28]. Each iteration increasingly fits the estimate to the noisy data in the maximum likelihood sense, leading to noise amplification after a number of iterations due to the lack of *a priori* knowledge of the scene statistics, or regularization. We limit the number of iterations to prevent excessive noise amplification.

In image recovery, we assume a three-fold increase in resolution from nine 213×213-pixel images to a super-resolved 639×639-pixel image, thus vectors $\mathbf{x}$ and $\mathbf{y}$ have 408321 elements, $\mathbf{y}_k$ have 45369 elements each, matrix $\mathbf{D}$ is of 45369×408321 elements, and matrices $\mathbf{H}_k$, $\mathbf{W}_k$ and system matrix $\mathbf{M}$ are of 408321×408321 elements each. Image recovery of simulated images, as described in the next section, was implemented in *Matlab*® and required 2.2 seconds for a 10-iteration restoration running on a current PC. Dedicated software, which would need to store the sparse matrix $\mathbf{M}$, would reduce recovery time by several orders of magnitude, enabling real-time operation.

C. Results

Here we compare the image quality predicted by simulations for the MA and baseline systems, under equivalent imaging conditions. The systems have similar focal ratios and, when imaging a natural scene, the number of photons per pixel is on average the same for both imaging systems (the optical étendues are equal: a pixel in the MA system subtends a solid angle in the object space that is nine times greater than in the baseline system, but with a ninth of the aperture area). Hence, recorded images of extended scenes will have similar Signal-to-Noise Ratio (SNR) levels. On the other hand, a difference is found for imaging of point sources (rather than extended sources) in the presence of strong aliasing. In this case, the total energy collected by a pixel in the MA system is approximately nine times smaller due to the reduced aperture but nine pixels will be responsive to each point source, reducing the potential for saturation of the detector elements at the cost of a reduced SNR. However, we assume the case of natural scenes in what follows and thus we assume the same SNR at the detector in both systems.

We use the root-mean-squared error, $\varepsilon_{\mathrm{RMS}}$, to assess the accuracy of the reconstructed image,

$$\varepsilon_{\mathrm{RMS}} = \frac{\sqrt{\sum\left(\hat{\mathbf{x}} - \mathbf{x}\right)^2}}{R\,n} \tag{6}$$

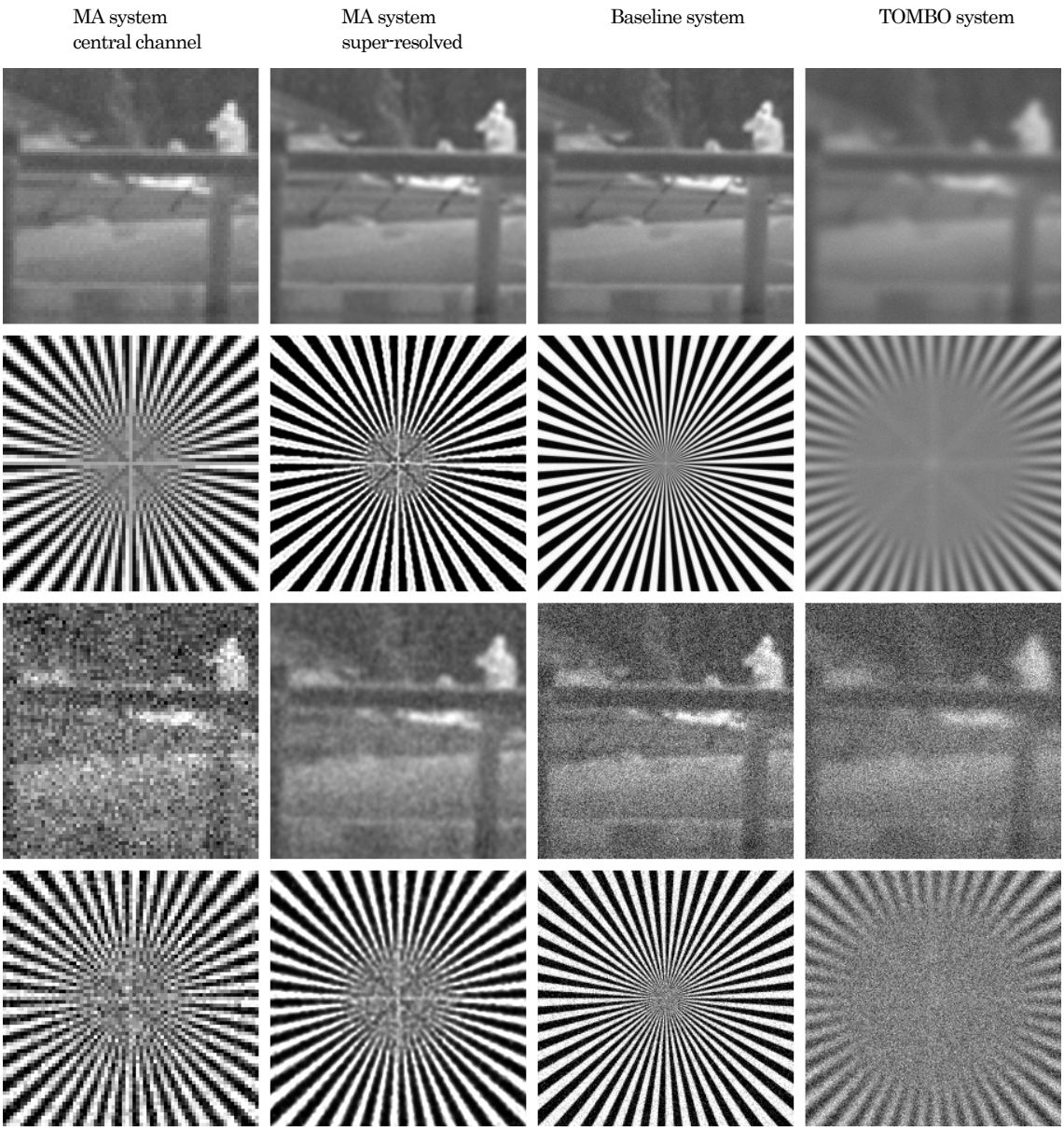

Fig. 8. Simulated images for zoomed-in images taken from (rows 1 and 3) the scene shown in Fig. 7 and (rows 2 and 4) a spoke target. Each column shows detail of (from left to righ): low-resolution image of the central channel, reconstructed image for the MA system, image acquired with the diffraction limited conventional system, and reconstruction results from a ideally-aligned TOMBO approach. Detected signal-to-noise ratio is 100:1 for the upper two rows and 10:1 for the lower two rows.

where R is the image dynamic range.

Images obtained from simulations of image acquisition and image restoration are shown in Fig. 8 using the scene in Fig. 7 and a spoke target, and for SNRs in the detected image of 40dB and 20dB. Comparison of the images in columns two and three demonstrates that super-resolution of the low-resolution images yields image resolution comparable to the baseline system. Thus comparable image quality is maintained whilst the system track length has been reduced by a factor four. Additionally, simulation results for a diffraction-limited TOMBO system (as depicted in Fig. 2(b)) are shown in column four which illustrate how, in this case of high-angular resolution imaging (that is, long focal length for the baseline imager), the reduced aperture size that results from the α=1 constraint (the lenslet width is constrained to be one-third of the detector width) leads to an appreciably lower system optical cutoff angular frequency and consequently lower system cutoff frequency in addition to a higher f-number. Results for the TOMBO approach are calculated using Fourier optics and the images are reconstructed using pixel rearrangement as the low-resolution images are ideally assumed to show (a) no distortion and (b) regularly spaced sampling phases.

To assess the robustness of image recovery, simulations were performed for a range of scene characteristics and SNR in the detected image. The scenes used in the simulations are shown in Fig. 9. The variation of ε_{RMS} in the recovered images is shown for 5, 20 and the optimum number of iterations (*i.e.* the number of iterations that minimizes ε_{RMS} in each case) in Fig. 9(a), Fig. 9(b) and Fig. 9(c). In optimizing image recovery, an agile trade of SNR against signal bandwidth is possible: that is image smoothing can yield a lower RMS image error. This is apparent in the plots in in Fig. 9(a) and Fig. 9(c) where suppression of noise by image smoothing (due to reduced iterations used in recovery) yields a

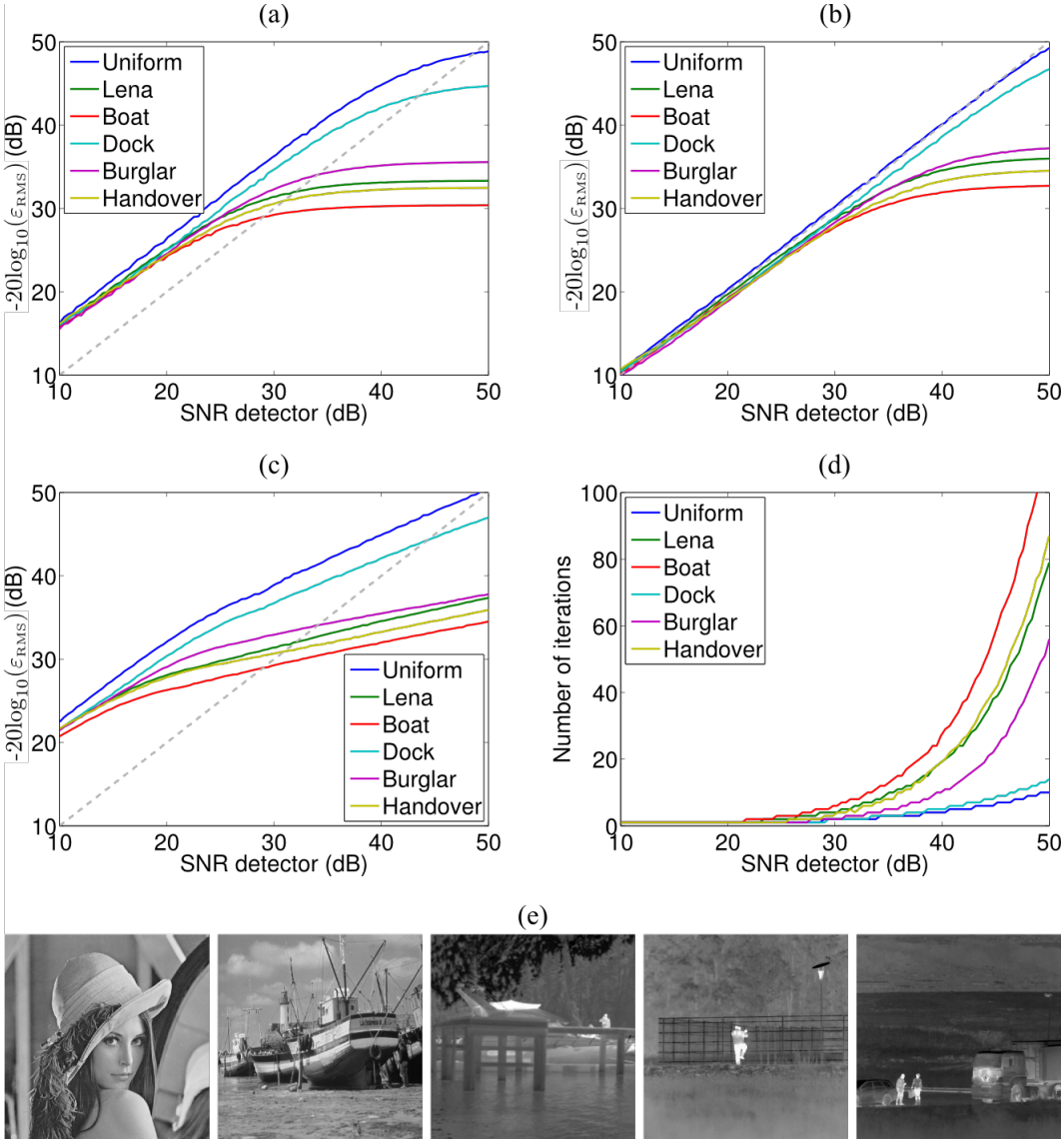

Fig. 9. Noise propagation; the graphs show how the SNR is altered by the system using (a) 5 iterations, (b) 20 iterations, and (c) the optimum number of iterations that minimizes ε_{RMS}, which varies as shown in (d). The set of images (e) are the scenes for which the calculations were performed referred to as 'Lena', 'Boat', 'Dock', 'Burglar' and 'Handover'; 'Uniform' corresponds to a uniform, unstructured scene intensity.

lower RMS error than the detected SNR. As can be seen from Fig. 9(b), for 20 iterations, ε_{RMS} is approximately equal to the detected SNR for SNR<30dB, but restoration artifacts, such as ringing, become increasingly apparent at higher SNRs. The optimal number of iterations is therefore influenced by application requirements.

This trade of SNR against image bandwidth can be appreciated by comparison of the images in Fig. 8: where the SNR at the detector is lower, the reconstructed images show reduced noise at the expense of reduction in image bandwidth. Note for instance how the maximum resolved frequency of the simulated spoke target is lower in the high-noise case but the output noise levels are reduced.

4. Conclusions

We have highlighted the limited scope for traditional approaches to MA imaging to provide a reduction in track length without sacrificing angular resolution and then described a new approach that enables the track-length reduction of MA imaging to be obtained with arbitrarily high angular resolution. In an example simulation of such a system, the optical design was optimized independently in each imaging channel to achieve diffraction-limited image resolution at the detector and detector-limited image resolution in each channel. With appropriate image processing these multiple images can be super-resolved to yield image quality comparable to that of a baseline system. As demonstrated here the advantage of this technique is an approximately N-fold reduction in track length with little compromise in image quality.

An additional important factor arises from the reduced contribution of geometrical aberrations as imaging systems are scaled to smaller dimensions, which results in an empirically-observed requirement for f-number to increase with focal length [29]. For the reduced focal lengths of MA imaging therefore, diffraction-limited space-bandwidth product, that is, the so-called Shannon limit [30] (of the lenslet), can be achieved from simpler low f-number lens systems. Our proposed technique requires the added complexity of off-axis lenslets, however in the regime of

long-wavelength infrared imaging for which we present a design solution, angular resolutions are typically relatively low (as identified in [29]) and so diffraction-limited, low f-number imaging can be achieved with relatively simple optics for both axial and off-axis imaging.

Two important *quid pro quo*s are the added complexity in the required off-axis optics and the computational load for image recovery, however these issues are tractable: free-form off-axis optics can be manufactured using single-point diamond machining and can be molded with reduced cost for imaging in the LWIR and the computational load for recovery is compatible with real-time operation when implemented with dedicated digital processing hardware and software. Importantly, the high sparsity of the system matrix means the computational load scales linearly with pixel count.

Acknowledgements
GC and GM are grateful to Qioptiq Ltd, St Asaph, Wales, and the Knowledge Transfer Partnership scheme for financial support.

References

1. J. Tanida, T. Kumagai, K. Yamada, S. Miyatake, K. Ishida, T. Morimoto, N. Kondou, D. Miyazaki, and Y. Ichioka, "Thin observation module by bound optics (TOMBO): Concept and experimental verification," Appl. Opt. **40**, 1806–1813 (2001).
2. A. Portnoy, N. Pitsianis, X. Sun, D. Brady, R. Gibbons, A. Silver, R. Te Kolste, C. Chen, T. Dillon, and D. Prather, "Design and characterization of thin multiple aperture infrared cameras," Appl. Opt. 48, 2115–2126 (2009).
3. A. Kanaev, J. Ackerman, E. Fleet, and D. Scribner, "TOMBO sensor with scene-independent superresolution processing," Opt. Lett. **32**, 2855–2857 (2007).
4. M. Shankar, R. Willett, N. Pitsianis, T. Schulz, R. Gibbons, R. Te Kolste, J. Carriere, C. Chen, D. Prather, and D. Brady, "Thin infrared imaging systems through multichannel sampling," Appl. Opt. 47, B1-B10 (2008).
5. K. Venkataraman, D. Lelescu, J. Duparré, A. McMahon, G. Molina, P. Chatterjee, R. Mullis, and S. Nayar, "PiCam: an ultra-thin high performance monolithic camera array," ACM Trans. Graph. 32, 166:1–166:13 (2013).
6. R. Horisaki, K. Kagawa, Y. Nakao, T. Toyoda, Y. Masaki, and J. Tanida, "Irregular Lens Arrangement Design to Improve Imaging Performance of Compound-Eye Imaging Systems," Appl. Phys. Expr. 3, 22501 (2010).
7. S. C. Park, M. K. Park, and M. G. Kang, "Super-resolution image reconstruction: a technical overview," IEEE Signal Processing Magazine **20**, 21–36 (2003).
8. J. Downing, E. Findlay, G. Muyo, and A. R. Harvey, "Multichanneled finite-conjugate imaging," J. Opt. Soc. Am. A **29**, 921–927 (2012).
9. L. Li and A.Y. Yi, "Design and fabrication of a freeform microlens array for a compact large-field-of-view compound-eye camera," Appl. Opt. 51, 1843-1852 (2012).
10. G. Druart, N. Guérineau, R. Haïdar, S. Thétas, J. Taboury, S. Rommeluère, J. Primot, and M. Fendler, "Demonstration of an infrared microcamera inspired by *Xenos peckii* vision," Appl. Opt. 48, 3368-3374 (2009).
11. J. Meyer, A. Brückner, R. Leitel, P. Dannberg, A. Bräuer, and A. Tünnermann, "Optical Cluster Eye fabricated on wafer-level," Opt. Express 19, 17506-17519 (2011).
12. K. Stollberg, A. Brückner, J. Duparré, P. Dannberg, A. Bräuer, and A. Tünnermann, "The Gabor superlens as an alternative wafer-level camera approach inspired by superposition compound eyes of nocturnal insects," Opt. Express 17, 15747-15759 (2009).
13. T. Georgiev, Z. Yu, A. Lumsdaine, S. Goma, "Lytro camera technology: theory, algorithms, performance analysis," Proc. of SPIE Multimedia Content and Mobile Devices, **8667**, 86671J-86671J10 (2013).
14. T. E. Bishop, P. Favaro, "The Light Field Camera: Extended Depth of Field, Aliasing, and Superresolution," IEEE Trans. Pattern Anal. Mach. Intell. **34**, 972–986 (2012).
15. K. Ohashi, K. Takahashi, T. Fujii, "Joint Estimation of High Resolution Images and Depth Maps from Light Field Cameras," Proc. of SPIE Stereoscopic Displays and Applications XXV, **9011**, 90111B-90111B-7 (2014).
16. S. Shroff and K. Berkner, "Image formation analysis and high resolution image reconstruction for plenoptic imaging systems," Appl. Opt. 52, D22-D31 (2013).
17. M. Broxton, L. Grosenick, S. Yang, N. Cohen, A. Andalman, K. Deisseroth, and M. Levoy, "Wave optics theory and 3-D deconvolution for the light field microscope," Opt. Express **21**, 25418-25439 (2013).
18. G. Carles, J. Downing and A. R. Harvey, "Super-resolution imaging using a camera array," Opt. Lett. **39**, 1889–1892 (2014).
19. M. Elad and A. Feuer, "Restoration of a single superresolution image from several blurred, noisy, and undersampled measured images," IEEE Transactions on Image Processing **6**, 1646–1658 (1997).
20. M. Elad and Y. Hel-Or, "A fast super-resolution reconstruction algorithm for pure translational motion and common space-invariant blur," IEEE Transactions on Image Processing **10**, 1187–1193 (2001).
21. S. Farsiu, M. D. Robinson, M. Elad, and P. Milanfar, "Fast and robust multiframe super resolution," IEEE Transactions on Image Processing **13**, 1327–1344 (2004).
22. M. Irani and S. Peleg, "Improving resolution by image registration," CVGIP: Graphical Models Image Process. **53**, 231–239 (1991).
23. M. Irani and S. Peleg, "Motion analysis for image enhancement: Resolution, occlusion, and transparency," Journal of Visual Communication and Image Representation **4**, 324–335 (1993).
24. R. R. Schultz and R. L. Stevenson, "Extraction of high-resolution frames from video sequences," IEEE Transactions on Image Processing **5**, 996–1011 (1996).
25. R. L. Lagendijk and J. Biemond, *Iterative identification and restoration of images* (Kluwer Academic Publishers, Boston, 1991).
26. J. L. Barron, D. J. Fleet, S. S. Beauchemin, and T. A. Burkitt, "Performance of optical flow techniques," International Journal of Computer Vision **12**, 43–77 (1994).
27. D. P. Bertsekas and D. P. Bertsekas, *Nonlinear Programming* (Athena Scientific, 1999), 2nd ed.
28. L. A. Shepp and Y. Vardi, "Maximum likelihood reconstruction for emission tomography," IEEE Transactions on Medical Imaging **1**, 113–122 (1982).
29. A. Lohmann, "Scaling laws for lens systems," Appl. Opt. 28, 4996-4998 (1989).
30. A. Stern and B. Javidi, "Shannon number and information capacity of three-dimensional integral imaging," J. Opt. Soc. Am. A, **21**, 1602-1612 (2004)